SHADE: A Multilevel Bayesian Framework for Modeling Directional Spatial Interactions in Tissue Microenvironments

Joel Eliason[*1], Michele Peruzzi[2], and Arvind Rao[1,2,3,4]

[1]Department of Computational Medicine and Bioinformatics, University of Michigan, USA

[2]Department of Biostatistics, University of Michigan, USA

[3]Department of Biomedical Engineering, University of Michigan, USA

[4]Department of Radiation Oncology, University of Michigan, USA

November 17, 2025

Abstract

Motivation: Understanding how different cell types interact spatially within tissue microenvironments is critical for deciphering immune dynamics, tumor progression, and tissue organization. Many current spatial analysis methods assume symmetric associations or compute image-level summaries separately without sharing information across patients and cohorts , limiting biological interpretability and statistical power.

---
[*]Corresponding author: joelne@umich.edu. Present address: Department of Biomedical Engineering, Johns Hopkins University, Baltimore, MD, USA.

1

Results: We present SHADE (Spatial Hierarchical Asymmetry via Directional Estimation), a multilevel Bayesian framework for modeling asymmetric spatial interactions across scales. SHADE quantifies direction-specific cell-cell associations using smooth spatial interaction curves (SICs) and integrates data across tissue sections, patients, and cohorts. Through simulation studies, SHADE demonstrates improved accuracy, robustness, and interpretability over existing methods. Application to colorectal cancer multiplexed imaging data reveals biologically meaningful spatial asymmetries in immune and stromal organization, underscoring SHADE's potential for translational insights.

Availability and Implementation: Open-source implementation is available at `https://github.com/jeliason/SHADE` and `https://github.com/jeliason/shade_paper_code`, developed in R and Stan.

Keywords: spatial statistics, cell-cell interactions, Bayesian modeling, tissue microenvironment, multiplex imaging, colorectal cancer

1 Introduction

Spatial dependencies between cell types play a central role in immune dynamics, tumor behavior, and tissue organization, motivating statistical models that can capture such interactions [??]. The tumor microenvironment (TME) is a spatially structured system where cell arrangements are closely linked to disease progression and treatment response [??]. Notably, these spatial interactions are frequently asymmetric: immune cells may cluster near tumor cells without the reverse being true, reflecting directional dependencies in tissue organization [?].

Recent advances in multiplexed imaging technologies, including multiplexed immunofluorescence (mIF) and other high-resolution spatial profiling methods, have made it possible to quantify cell type spatial distributions and interactions within the tumor microenvironment (TME) at single-cell resolution [?]. Benchmarking studies have compared classical spatial

summary statistics (Ripley's K-function, G-cross) for detecting co-localization in mIF and IMC data [?], while functional data analysis methods such as mxfda [?] apply multilevel functional PCA to spatial summary statistics, decomposing variation across hierarchical levels without imposing parametric models on point patterns. While such methods effectively characterize dominant modes of variation in marginal pairwise associations [?], they do not model conditional relationships or enable joint estimation with partial pooling at the point process level.

Although Gibbs point process models offer a more flexible probabilistic framework [??], standard formulations assume symmetric interactions. While hierarchical Gibbs models have been proposed to accommodate directionality [??], standard implementations depend on parametric interaction functions that impose restrictive assumptions. Observations based on the G-cross function suggest that spatial interactions between cell types are inherently asymmetric [?], motivating statistical models that directly account for directional spatial effects.

In this work, we develop a flexible statistical framework for modeling asymmetric spatial associations in tissue microenvironments. Our approach extends multitype Gibbs point process models [???] by modeling directional associations via *spatial interaction curves (SICs)* using flexible basis expansions within a multilevel Bayesian hierarchical structure. SICs quantify how the presence of one cell type relates to the expected density of another across spatial scales by modeling the *conditional intensity function*. Full posterior inference enables simultaneous credible bands for SICs and explicit quantification of spatial heterogeneity at each biological scale. Technical comparison with Gibbs models is provided in Supplement Section 1.

Beyond asymmetry, our method accounts for multilevel variation across images, patients, and cohorts. Biological spatial patterns vary at multiple levels, yet standard spatial summary statistics such as Ripley's K-function and the G-cross function compute estimates separately for each image without explicit hierarchical structure [??], limiting their ability to formally

model and partition heterogeneity across biological scales. While such methods can describe variability by computing per-image statistics, they do not enable joint estimation with partial pooling or explicit decomposition of variance components across images, patients, and cohorts . We integrate the estimation of SICs into a multilevel Bayesian framework, which enables partial pooling across biological scales while preserving biologically meaningful variation. This hierarchical structure allows SHADE to explicitly quantify and compare spatial heterogeneity at each level (Section 4.3), improving estimation efficiency while maintaining interpretable decomposition of variation.

To ensure computational efficiency, we approximate conditional intensity estimation using logistic regression with quadrature-based dummy points rather than direct Poisson likelihood estimation [**?**]. This transformation avoids computational challenges such as instability in fine-grained quadrature approximations and biases inherent in conventional spatial regression techniques.

We refer to this overall modeling framework as SHADE (Spatial Hierarchical Asymmetry via Directional Estimation). An overview of the SHADE workflow is provided in Figure 1.

2 Methods

2.1 Hierarchical Modeling of Conditional Spatial Point Processes

We model the spatial distribution of a target cell type B given the presence of one or more conditioning cell types $A_1, A_2, \ldots, A_K$, using a hierarchical framework based on conditional spatial point processes. Our approach extends hierarchical Gibbs models [**??**] and is designed to flexibly estimate asymmetric spatial association patterns while accounting for multilevel variation across images, patients, and cohorts.

Let $X_{A_k}, X_B \subset W$ denote the observed spatial point patterns of cell types A_k and B, respectively, within a two-dimensional tissue region $W \subset \mathbb{R}^2$. Formally, $X_{A_k} = \{x_i^{(k)} \in W \mid i = 1, \ldots, N_{A_k}\}$, $X_B = \{y_j \in W \mid j = 1, \ldots, N_B\}$, where $x_i^{(k)} = (x_{i1}^{(k)}, x_{i2}^{(k)}) \in \mathbb{R}^2$ denotes
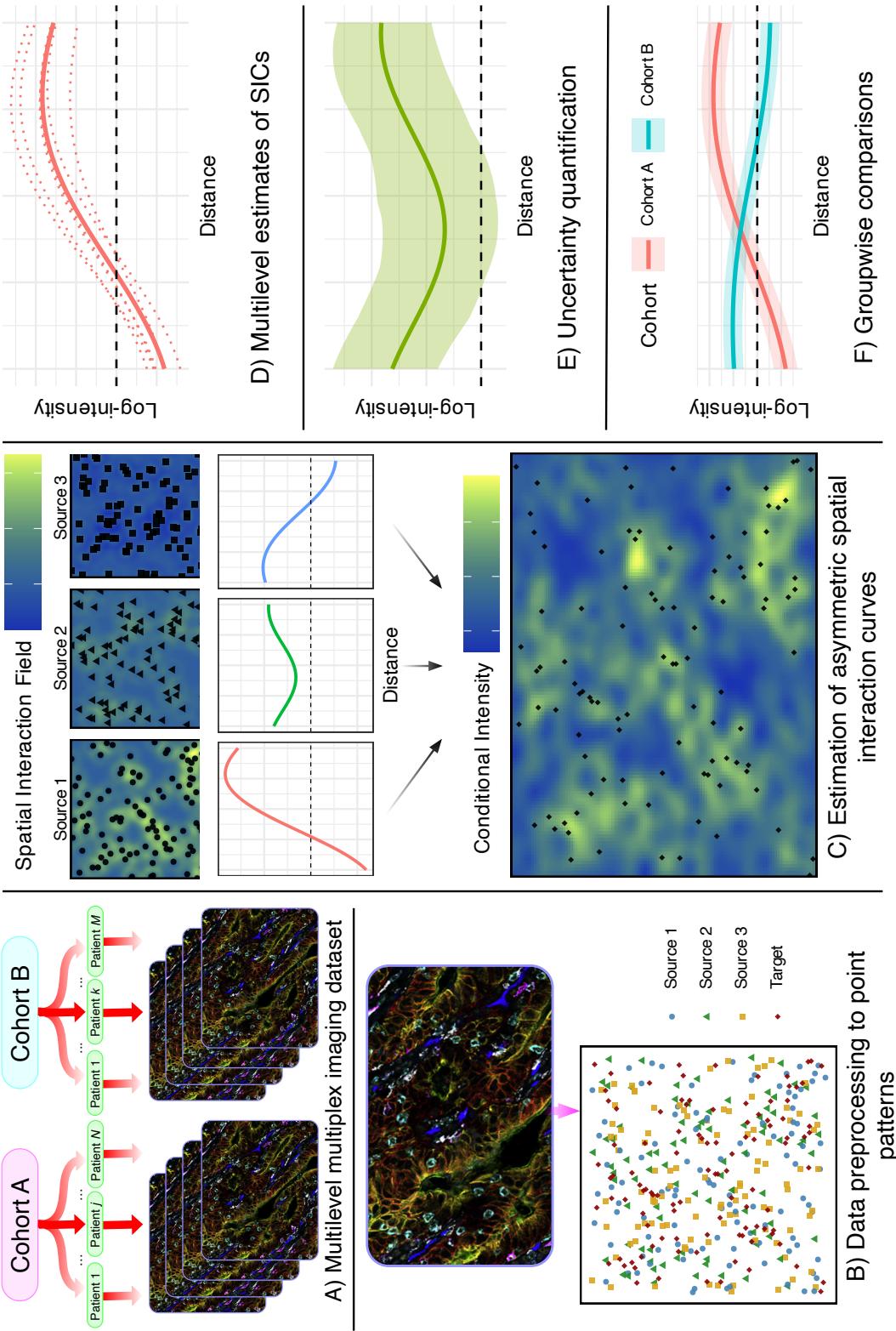
Figure 1: Summary of the SHADE (Spatial Hierarchical Asymmetry via Directional Estimation) framework. **A)** Multiplexed imaging data is structured hierarchically across cohorts, patients, and images. Multiplex images were adapted from **?** and are used under a Creative Commons CC BY 4.0 license. **B)** Images are processed into spatial point patterns with cell type annotations. **C)** SHADE estimates Spatial Interaction Curves (SICs) that capture directional associations between cell types across spatial scales. **D)** SICs are estimated at cohort, patient, and image levels, enabling multilevel analysis of spatial heterogeneity. **E)** Posterior distributions provide uncertainty quantification. **F)** SICs can be compared across cohorts to assess differences in spatial organization.

5

the two-dimensional spatial coordinate of the i-th cell of type A_k, and $y_j = (y_{j1}, y_{j2}) \in \mathbb{R}^2$ denotes the coordinate of the j-th cell of type B. The quantities N_{A_k} and N_B indicate the total number of observed cells of type A_k and B, respectively. The observation window W corresponds to the region of tissue captured in the image, typically a rectangular subset of the plane defined by the image dimensions.

In practice, X_{A_k} and X_B are obtained from image segmentation and cell type classification pipelines applied to high-resolution tissue images, such as those generated by multiplexed imaging platforms.

We model the spatial distribution of X_B (the *target* cell type, e.g., immune cells) conditional on $X_{A_1}, \ldots, X_{A_K}$ (the *source* cell types, e.g., tumor cells and vasculature) by assuming that $X_B \mid X_{A_1}, \ldots, X_{A_K}$ follows an inhomogeneous Poisson point process [**?**]. This allows the expected density of target cells to vary flexibly across space as a function of source cell locations and covariates, enabling the framework to represent complex spatial patterns including clustering, repulsion, and distance-dependent associations. While alternative models exist (e.g., Cox processes, cluster processes, Gibbs processes), the inhomogeneous Poisson process provides the best balance of flexibility, interpretability, and computational feasibility for our application [**?**]. The likelihood is:

$$L(X_B \mid X_{A_1}, \ldots, X_{A_K}) = \left[\prod_{v \in X_B} \lambda(v \mid X_{A_1}, \ldots, X_{A_K}) \right] \times \exp\left(-\int_W \lambda(v \mid X_{A_1}, \ldots, X_{A_K}) \, dv \right), \tag{1}$$

where the product runs over all observed locations of type B, while the integral accounts for the total expected intensity over the observation window W. The point process for X_B is entirely characterized by its *conditional intensity function* $\lambda(v \mid X_{A_1}, \ldots, X_{A_K})$, which defines the expected local density of type B cells at any location $v \in W$, conditioned on the spatial configurations of the conditioning cell types, that is, $\lambda(v \mid X_{A_1}, \ldots, X_{A_K}) = \lim_{|dv| \to 0} \frac{1}{|dv|} E[N_B(dv) \mid X_{A_1}, \ldots, X_{A_K}]$.

We model $\lambda(\cdot)$ as depending log-linearly on the observed patterns of $A_1, \ldots, A_K$ cells:

$$\log \lambda(v \mid X_{A_1}, \ldots, X_{A_K}) = \boldsymbol{z}^\top(v)\boldsymbol{\beta} + \sum_{k=1}^{K} \boldsymbol{q}_{A_k}^\top(v)\boldsymbol{\psi}_{A_k} \tag{2}$$

In (2), the term $\boldsymbol{z}(v) \in \mathbb{R}^J$ is a vector of covariates at location v (including an intercept), with corresponding coefficients $\boldsymbol{\beta} \in \mathbb{R}^J$. The vector $\boldsymbol{q}_{A_k}(v) \in \mathbb{R}^P$ encodes spatial interaction features between type A_k and type B; its p-th element is defined as:

$$[\boldsymbol{q}_{A_k}(v)]_p = \sum_{x \in X_{A_k}} \phi_p\left(\mathrm{dist}(v, x)\right), \tag{3}$$

where $\phi_p(\cdot)$ is a basis function (e.g., a B-spline or Gaussian kernel) that modulates the influence of a type A_k cell at a given distance from v. Finally, $\boldsymbol{\psi}_{A_k} \in \mathbb{R}^P$ are the corresponding coefficients. This formulation flexibly captures how proximity to different cell types influences the expected density of type B cells across spatial scales. Our use of smooth interaction features in (3) reflects biologically realistic, distance-dependent associations. In doing so, we generalize traditional Gibbs process formulations by avoiding rigid parametric forms such as fixed interaction radii [?], which fail to capture the continuous and often subtle variations observed in biological spatial interactions [?].

While the model specified in (2) provides a flexible representation of spatial interactions through basis expansions, directly interpreting the estimated coefficients $\boldsymbol{\psi}_{A_k}$ can be difficult. In particular, biological interest often centers on how the strength and direction of association between a conditioning cell type A_k and a target cell type B vary as a function of distance. To facilitate interpretable biological insights, we next define a derived quantity, the *spatial interaction curve* (SIC), which summarizes the estimated effect of proximity to A_k cells on the expected density of B cells across spatial scales.

2.1.1 Spatial Interaction Curve

The SIC summarizes the asymmetric spatial association between a conditioning cell type A_k and a target cell type B as a function of distance s:

$$\text{SIC}_{A_k \to B}(s) = \sum_{p=1}^{P} \psi_{A_k}^{(p)} \phi_p(s), \tag{4}$$

This curve represents the expected contribution of type A_k cells to the log-intensity of type B cells as a function of distance s from a type A_k cell. Here, log-intensity refers to the logarithm of the conditional intensity function $\lambda(v)$ (Equation 2), which describes the expected spatial density of type B cells (in cells per unit area) at any location v. Because the model is log-linear, SIC values quantify additive changes on the log-intensity scale, which correspond to multiplicative changes in actual cell density. For example, $\text{SIC} = 0.2$ at distance s implies an $e^{0.2} \approx 1.22\times$ (or 22%) increase in the expected local density of type B cells at radius s from a type A_k cell, while $\text{SIC} = -0.3$ corresponds to an $e^{-0.3} \approx 0.74\times$ decrease (26% reduction).
.

As illustrated in Figure 2, a positive SIC value at distance s indicates that the presence of a type A_k cell is associated with an increased expected density of type B cells at that radius, consistent with spatial attraction or clustering. Conversely, a negative SIC value suggests spatial repulsion or avoidance at that distance. This function provides an interpretable, distance-dependent summary of directional spatial association between cell types. Additional explanation of the SIC is contained in the Supplement.

Because cell centroids cannot occur arbitrarily close in space, very short distances (below approximately 1-2 cell diameters) can reflect geometric crowding, cell-cell contact, or segmentation artifacts, making biological interpretation ambiguous. We therefore predefine a minimum interaction radius $r_{\min} = 25$ μm (approximately 1.5-2 typical cell diameters) and report spatial interaction curves only for $r \geq r_{\min}$. The model is fit using all observed cell locations, but posterior summaries and spatial interaction curves are evaluated and reported

only at distances $r \geq r_{\min}$ to focus interpretation on unambiguous intercellular spacing. All band-level posterior probabilities are computed on intervals $I \subseteq [r_{\min}, \infty)$.
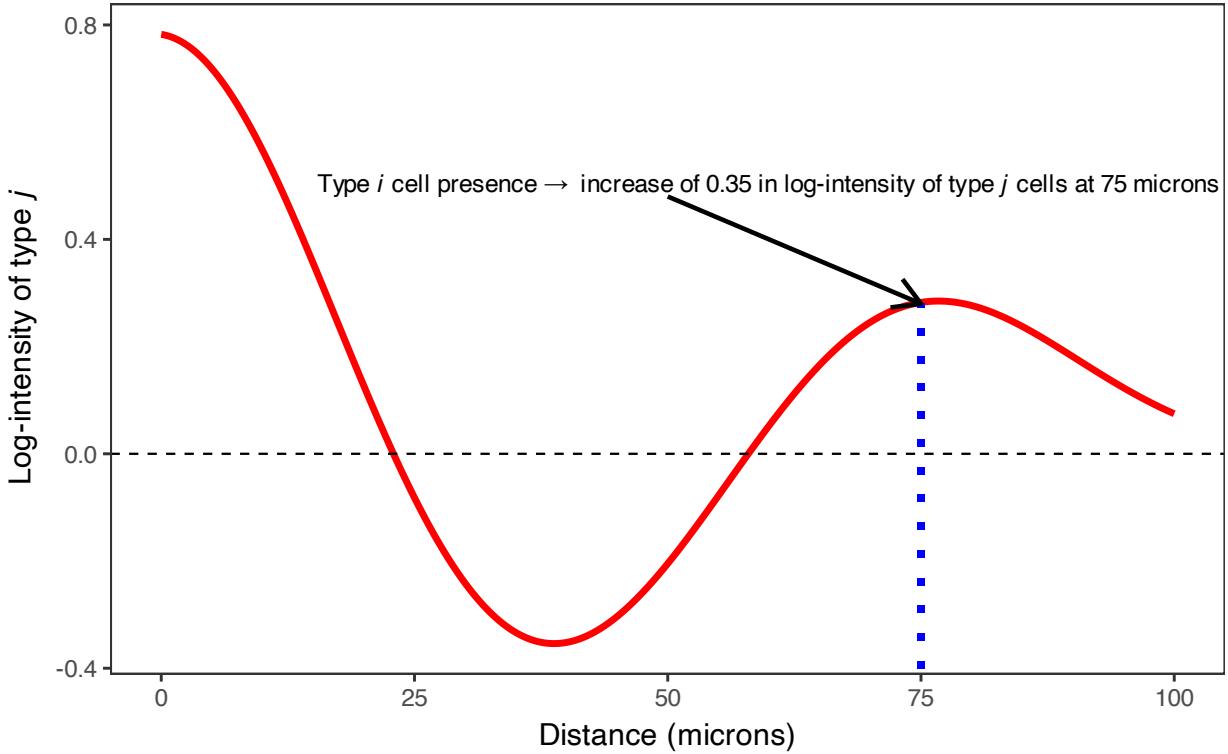

Figure 2: An example spatial interaction curve showing the effect of a source cell type A_k on a target cell type B, with simultaneous 95% credible bands. At each distance s, the curve value represents the change in log-intensity of type B associated with the presence of a type A_k cell at distance s.

A key advantage of our framework is that the spatial interaction terms $\boldsymbol{\psi}_{A_k}$ can take both positive and negative values, allowing for flexible modeling of attraction and repulsion. This mirrors the flexibility of hierarchical Gibbs models while overcoming constraints in symmetric pairwise interaction models, which typically restrict interaction terms to be non-positive and therefore cannot directly model spatial attraction.

2.1.2 Characterizing Predictive Asymmetry

Our modeling framework captures *predictive* spatial associations, not biological causation. A strong $A \rightarrow B$ SIC indicates that the presence of A is statistically predictive of local B

density, meaning that the spatial locations of type A cells provide information about where type B cells are likely to be found. Formally, this means that the conditional intensity function $\lambda(v \mid X_A)$ differs from the marginal (unconditional) intensity $\lambda_B(v)$, which represents the expected density of type B cells in the absence of any spatial dependence on type A locations. Under complete spatial independence, knowing where type A cells are located provides no information about type B density, so $\lambda(v \mid X_A) = \lambda_B(v)$.

Importantly, while our model quantifies the strength and direction of spatial predictability, it does not establish that A exerts a causal biological effect on B. Apparent directional associations may arise from confounding factors such as differences in the spatial distribution of A (e.g., sparser, more clustered, or more localized patterns), which can make A a stronger statistical predictor without implying direct biological influence.

To mitigate such confounding, the model can incorporate spatial covariates or trend surfaces (e.g., distance to the tumor margin) to adjust for first-order intensity effects. This adjustment ensures that estimated directional SICs capture residual spatial association beyond shared background structure.

2.2   Multilevel Bayesian Model

To capture biological variability across individuals and sampling levels, we impose a hierarchical prior structure on the spatial interaction coefficients. For each conditioning cell type A_k, the interaction coefficients are indexed hierarchically across three levels: cohort (ψ), patient (γ), and image (δ). Specifically, for each basis function p, we define:

$$
\begin{aligned}
\psi_{A_k}^{(g,p)} &\sim \mathcal{N}(0, \sigma_{\text{cohort}}^2), \\
\gamma_{A_k}^{(n,p)} &\sim \mathcal{N}(\psi_{A_k}^{(g(n),p)}, \sigma_{\text{patient}}^2), \\
\delta_{A_k}^{(m,p)} &\sim \mathcal{N}(\gamma_{A_k}^{(n(m),p)}, \sigma_{\text{image}}^2),
\end{aligned}
\tag{5}
$$

where $g(n)$ maps patient n to its cohort, and $n(m)$ maps image m to its corresponding patient. Each image-level coefficient $\delta_{A_k}^{(m,p)}$ governs the localized effect of source cell type A_k

10

on target cell type B at distance scale p, within image m.

This hierarchical formulation enables partial pooling across the dataset structure, improving estimation stability while preserving biologically meaningful heterogeneity in spatial interactions. By modeling variation at the cohort, patient, and image levels, the framework supports inference on both shared and context-specific spatial association patterns. When comparing spatial organization across biological groups (e.g., treatment responders vs. non-responders, different tumor subtypes), each group is modeled as a separate cohort with its own cohort-level parameters $\psi_{A_k}^{(g,p)}$. Differences between groups are then assessed by comparing the posterior distributions of these cohort-level parameters, as quantified through SICs (Equation 4) and their associated simultaneous credible bands.

Hyperpriors for the variance components σ_{cohort}^2, $\sigma_{\text{patient}}^2$, and σ_{image}^2 are detailed in the Supplement.

2.3 Uncertainty Quantification and Prioritization of Cell Type Pairs

To quantify uncertainty in estimated SICs and assess statistical significance, we employ simultaneous 95% credible bands that account for multiple comparisons across the distance domain. Unlike pointwise credible intervals, simultaneous bands provide joint coverage across all distances within a specified range, offering stronger protection against false discoveries. Statistical significance can be assessed by examining whether the simultaneous band excludes zero over a distance range of interest. Full implementation details are provided in the Supplement (Section 3.1).

In exploratory analyses involving many cell type pairs ($K(K-1)$ directed pairs for K cell types), we propose summary measures to facilitate prioritization: peak location and magnitude (identifying where the strongest interaction occurs), persistence over biologically relevant distance ranges (quantifying consistent associations within pre-specified intervals), and overall strength (integrating absolute effect sizes over significant regions). These measures

11

can be computed across all source–target pairs and visualized as heatmaps for systematic comparison. Formal definitions are provided in the Supplement (Section 3.2).

2.4 Logistic Regression Approximation for Computational Efficiency

Direct estimation of the Poisson likelihood in spatial point process models typically requires numerical integration over a fine spatial grid, which becomes computationally expensive and unstable in high-resolution images. To address this, we follow the logistic regression approximation introduced by **?**, which avoids spatial gridding by introducing a set of dummy points D sampled from a homogeneous Poisson process with known intensity λ_{dummy}. We define the combined set of points $Y = X_B \cup D$, and assign binary labels:

$$
I(v) = \begin{cases} 1, & v \in X_B \\ 0, & v \in D \end{cases}
$$

The conditional probability that a point v is a true (observed) point of type B is given by:

$$
P(I(v) = 1) = \frac{\lambda(v)}{\lambda(v) + \lambda_{\text{dummy}}},
$$

leading to the following logistic regression model:

$$
\log \frac{P(I(v) = 1)}{P(I(v) = 0)} = \boldsymbol{z}^\top(v)\boldsymbol{\beta} + \sum_{k=1}^{K} \boldsymbol{q}_{A_k}^\top(v)\boldsymbol{\delta}_{A_k}^{(m)} - \log \lambda_{\text{dummy}}, \tag{6}
$$

This approximation circumvents key computational challenges of direct Poisson modeling. In Poisson models, fine spatial discretization leads to large numbers of empty pixels, often resulting in singular design matrices and unstable inference [**?**]. The Hauck-Donner effect [**?**] can further distort uncertainty estimates. By reframing the problem as a binary classification

task over observed and dummy points, the logistic approximation enables scalable, stable inference of spatial interaction effects at the image level.

2.5   Model Estimation and Computational Implementation

Model fitting is implemented in `Stan` using Hamiltonian Monte Carlo (HMC) via `cmdstanr` [??].

To approximate the likelihood, we first generate a set of dummy points D from a homogeneous Poisson process with intensity λ_{dummy} over the observation window W. For each location $v \in X_B \cup D$, we then compute spatial covariates $\boldsymbol{z}(v)$ and interaction features $\boldsymbol{q}_{A_k}(v)$, where each interaction feature encodes basis-function-weighted distances to cells of type A_k.

Feature construction for each focal cell type B involves evaluating inter-cell distances between observed and dummy focal locations and all non-focal cells. This step scales as $\mathcal{O}(n_{\text{focal}} \times n_{\text{source}})$, which is quadratic in the total number of cells when the focal and source sets are of similar size. However, this operation is implemented using the optimized `crossdist` routine from `spatstat.geom`, which efficiently computes pairwise distances in compiled code. The resulting distance matrix is reused across all basis functions $\{\phi_p\}$ and source types $\{A_k\}$, so the dominant cost occurs only once per focal type.

To assess the practical runtime implications, we performed a timing experiment varying the total number of cells from 5,000 to 250,000 using variational inference (Supplement, Section 3.8). Feature construction time scaled as $O(n^{1.46})$ (empirical exponent from log-log regression), while total model fitting time scaled as $O(n^{0.85})$ due to efficient distance matrix reuse. At 100,000 cells, total fitting time was approximately 36 seconds; at 250,000 cells, approximately 133 seconds. These benchmarks demonstrate that SHADE remains computationally tractable for large-scale multiplexed imaging studies.

Using these constructed features, we fit a multilevel Bayesian logistic regression model based on the approximation in (6), with spatial interaction coefficients $\boldsymbol{\delta}_{A_k}^{(m,p)}$ modeled hierarchically according to the priors in (5). Finally, we extract posterior draws of the interaction

13

coefficients and reconstruct the spatial interaction curves using (4).

3   Simulation Studies

To evaluate the proposed model, we conducted simulation studies generating synthetic spatial point patterns that incorporated asymmetric interactions and multilevel structure. Spatial patterns were simulated within a bounded domain $W = [0, S] \times [0, S]$, with source points generated from a homogeneous Poisson process and target points influenced by spatial interaction curves defined over source-target distances. Hierarchical structure was introduced via interaction coefficients generated according to (5).

The final point pattern was converted into a logistic regression dataset using dummy points sampled from a homogeneous Poisson process with intensity λ_{dummy}, and spatial interaction features were computed as in (3). Full simulation details, including two additional studies exploring the effect of various hyperparameters on statistical inference, are provided in the Supplement.

3.1   The effect of explicitly modeling multilevel structure

In our first simulation study, we examined how accounting for hierarchical structure affects inference quality. We simulated data from two patient groups, each with 20 patients and 4 images per patient. Each image contained 150 points of each type, with a dummy-to-real point ratio of 2. The remaining parameters were set to defaults (see Supplement).

We generated 100 simulation replicates and fit two models to each: the full hierarchical model and a non-hierarchical model that estimates image-level SICs independently, without shrinkage to patient- or cohort-level structures. Inference quality was assessed by comparing the average RMSE of the $\delta_{t_1 \to t_2}^{(m,p)}$ coefficients.

We found that on average, and across all spatial scales, the average RMSE of $\delta_{t_1 \to t_2}^{(m,p)}$ coefficients was lower for those estimated by the full hierarchical model than the model that

fit images individually, most significantly so for closer-range coefficients (Table 1).

Hierarchical	Scale: All	Scale: Small	Scale: Medium	Scale: Large
False	0.142 (0.097, 0.196)	0.355 (0.230, 0.509)	0.022 (0.016, 0.031)	0.048 (0.034, 0.066)
True	0.039 (0.027, 0.043)	0.072 (0.043, 0.084)	0.017 (0.013, 0.020)	0.028 (0.021, 0.036)

Table 1: Average RMSE of $\delta_{t_1 \to t_2}^{(m,p)}$ coefficients in aggregate and across spatial scales, from both a model that fully accounts for the hierarchical structure as well as a model that does not account for hierarchy.

Figure 3 shows several examples of image-level SICs estimated with both models from this simulation study. In all cases, we can see that the SIC is better estimated when hierarchical structure is accounted for, in terms of both the bias and and variance of the estimate.
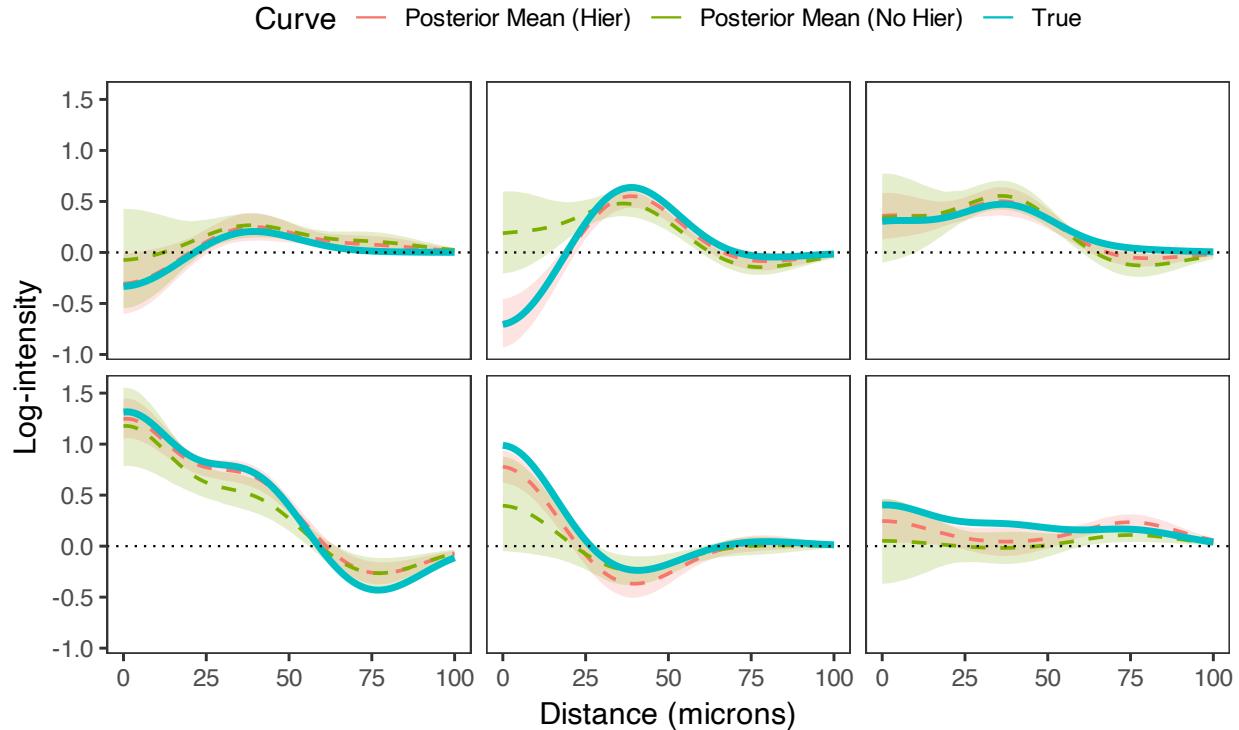
Figure 3: Examples of estimated image-level SICs from hierachical modeling simulations, with simultaneous 95% credible bands, demonstrating better estimation of SICs when accounting for multilevel structure.

3.2 Comparison of spatial pattern detection accuracy across methods

We conducted a simulation study to evaluate SHADE's detection power and calibration against established spatial analysis methods. We generated hierarchical spatial point patterns with known positive spatial interactions between T cells and tumor cells, modeling a single patient cohort with attraction patterns across multiple distance scales.

These simulations focus on *image-level* detection capabilities—the ability to identify spatial interactions within individual tissue sections using envelope-based methods. While SHADE's hierarchical framework enables inference at multiple biological scales (image, patient, and cohort levels), we compare here against G-cross and K-cross envelope tests that assess significance via completely spatially random (CSR) simulations. In Section 4.7, we present a complementary analysis comparing SHADE's group-level inference with functional data analysis methods that analyze marginal pairwise summary statistics.

We simulated spatial point patterns with patient- and image-level hierarchical structure (40 patients, 1–3 images per patient) using radial basis functions to model positive spatial interactions at short-, medium-, and long-range scales. We varied source cell density (the conditioning cell type: 15 vs. 150 cells per image) and target cell density (the cell type being modeled: 15 vs. 150 cells per image) across 50 replicates per condition. This design allows assessment of how SHADE's hierarchical pooling performs when the conditioning information is sparse versus abundant, and when multiple images per patient are available for information sharing. Detection power was evaluated as the proportion of simulations in which the method correctly identified that the spatial interaction curve differs from zero anywhere in the 0–75 μm range. For SHADE, detection was based on whether 95% simultaneous credible bands (see Supplement, Section 3.1) excluded zero at any distance. For comparison, we evaluated three baseline approaches: (1) G-cross envelope tests [?], testing whether the observed nearest-neighbor distribution falls outside 95% global envelopes constructed from 99 completely spatially random (CSR) simulations; (2) K-cross (specifically, L-cross) envelope

tests, using cumulative counts rather than nearest-neighbor distances; and (3) a 'Flat' model that estimates SICs independently for each image without hierarchical pooling. Type I error rates were assessed using null simulations with zero spatial interactions. Figure 4 illustrates one simulated example; full simulation details are provided in the Supplement.
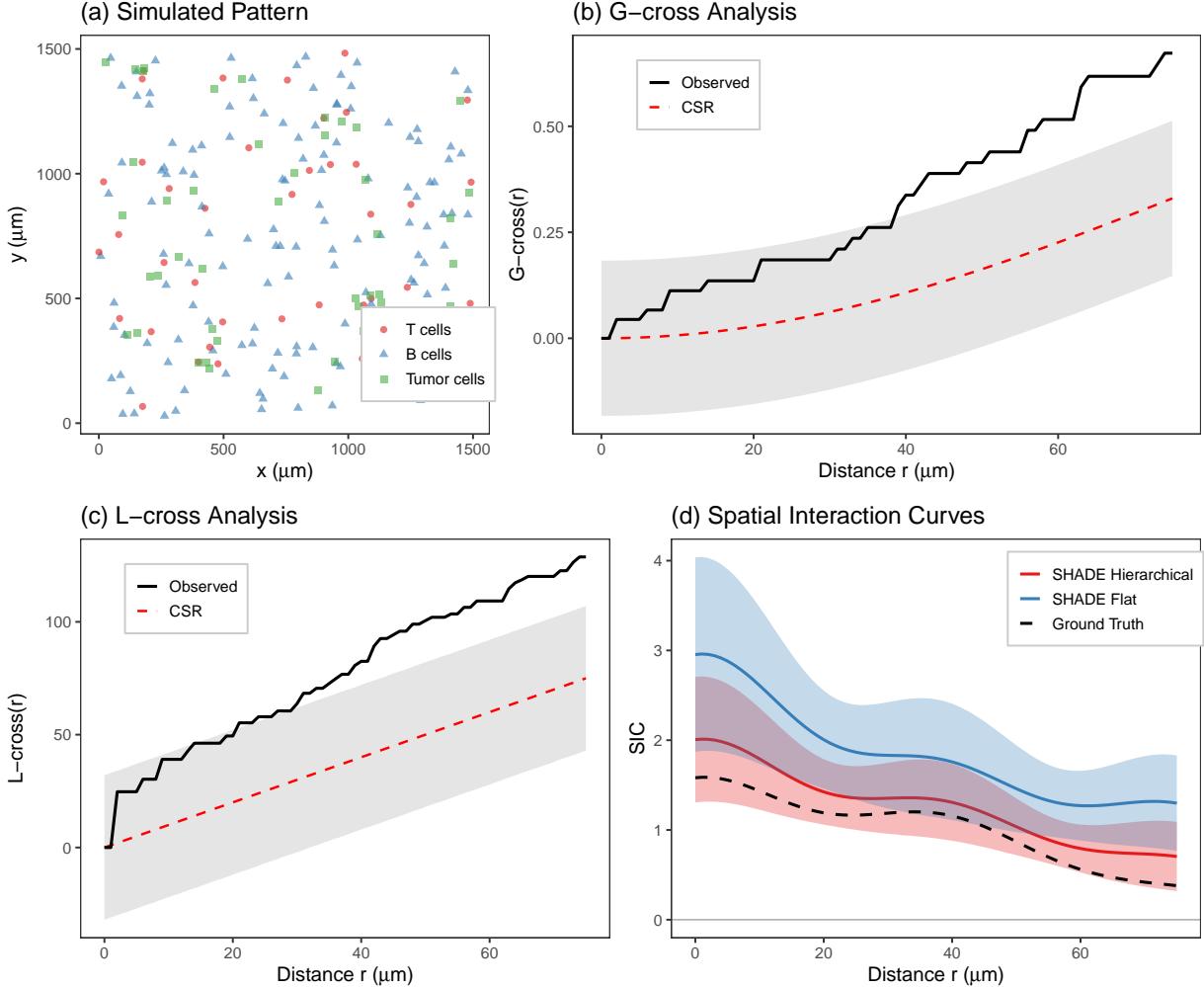

Figure 4: Simulation study comparing spatial analysis methods. (a) Simulated pattern showing T cells, B cells, and tumor cells in a $1500 \times 1500 \ \mu m^2$ region with known spatial clustering. (b) G-cross analysis with the observed curve (black), CSR expectation (dashed red), and 95% global envelope (gray ribbon) from 99 CSR simulations. (c) L-cross analysis, which counts all tumor cells within distance r of a typical T cell rather than measuring nearest-neighbor distances. (d) SIC estimates from SHADE Hierarchical (red), SHADE Flat (blue), and the ground truth (black dashed), with simultaneous 95% credible bands.

Figure 5 shows detection power across simulation conditions, where power is defined

as the proportion of simulated datasets in which the method correctly identifies that the spatial interaction curve differs from zero. Results reveal that SHADE Hierarchical's performance depends critically on two factors: source cell density (which provides conditioning information) and the number of images available for hierarchical pooling.

Effect of source density. When source density is high (regardless of target density), SHADE achieves excellent median power (100%) across all conditions, substantially outperforming envelope tests when target density is low (SHADE 100% vs. G-cross 77%, K-cross 73%). Abundant source cells provide strong conditioning information that hierarchical pooling can effectively leverage. Conversely, when source density is low, performance depends on whether multiple images are available: with 2–3 images per patient, median power reaches 100%; with only 1 image, power drops to 31% as limited conditioning information per image prevents effective pooling.

Effect of number of images. SHADE Hierarchical requires at least 2 images per patient for stable performance. With only 1 image per patient, the method exhibits extreme behavior: overly conservative under some conditions (100% coverage, 0% type I error when target density is high and source density is low) and unreliable under others (0% power with high type I error variability when both densities are low). With 2–3 images, performance stabilizes substantially, achieving high power when source density is adequate while maintaining reasonable calibration.

Most challenging scenario. When both source and target densities are low, all methods struggle. With 2–3 images per patient, SHADE achieves 26–28% median power with 94% coverage and well-controlled type I error (4%), demonstrating appropriate conservatism. G-cross performs best in this regime (49% power), likely because its nonparametric approach requires fewer assumptions about the data-generating process.

Coverage and type I error performance (Supplement Section 3.9) reveal adaptive calibration. When source density is high (favorable for detection), SHADE trades calibration for sensitivity (55% coverage, 100% power, <1% type I error). When both densities are

18

low (unfavorable for detection), SHADE becomes appropriately conservative (94% coverage, 28% power, 4% type I error). This contrasts with SHADE Flat, which maintains poor coverage (73%) regardless of scenario and shows severely inflated type I error rates (28%). Median type I error rates for SHADE Hierarchical with 2–3 images are well-controlled (0.8–7.5%), comparable to envelope tests (G-cross: 2.5–8.8%; K-cross: 1.3–6.7%), though with higher variability (IQR up to 0.12), indicating occasional liberal inference under challenging conditions.

Robustness to spatial confounding. We also tested SHADE's performance when the model is misspecified due to unmeasured spatial heterogeneity—specifically, discrete tissue compartments (e.g., tumor islands, stromal regions) that create baseline density differences independent of source-target interactions (Figure 6; Supplement Section 3.10). Results reveal regime-dependent bias: when both cell types are abundant, SHADE achieves perfect detection power but exhibits elevated Type I error rates (11.7–17.1%) and severely undercovers (43–52% vs. expected 95%), incorrectly attributing compartment effects to source-target interactions. When target density is low, wider credible bands provide partial robustness (82–93% coverage, 1.7–5.8% Type I error). These findings indicate that unmeasured spatial structure can produce substantial bias in high-density scenarios, suggesting the need for explicit compartment modeling or sensitivity analyses when such heterogeneity is suspected.
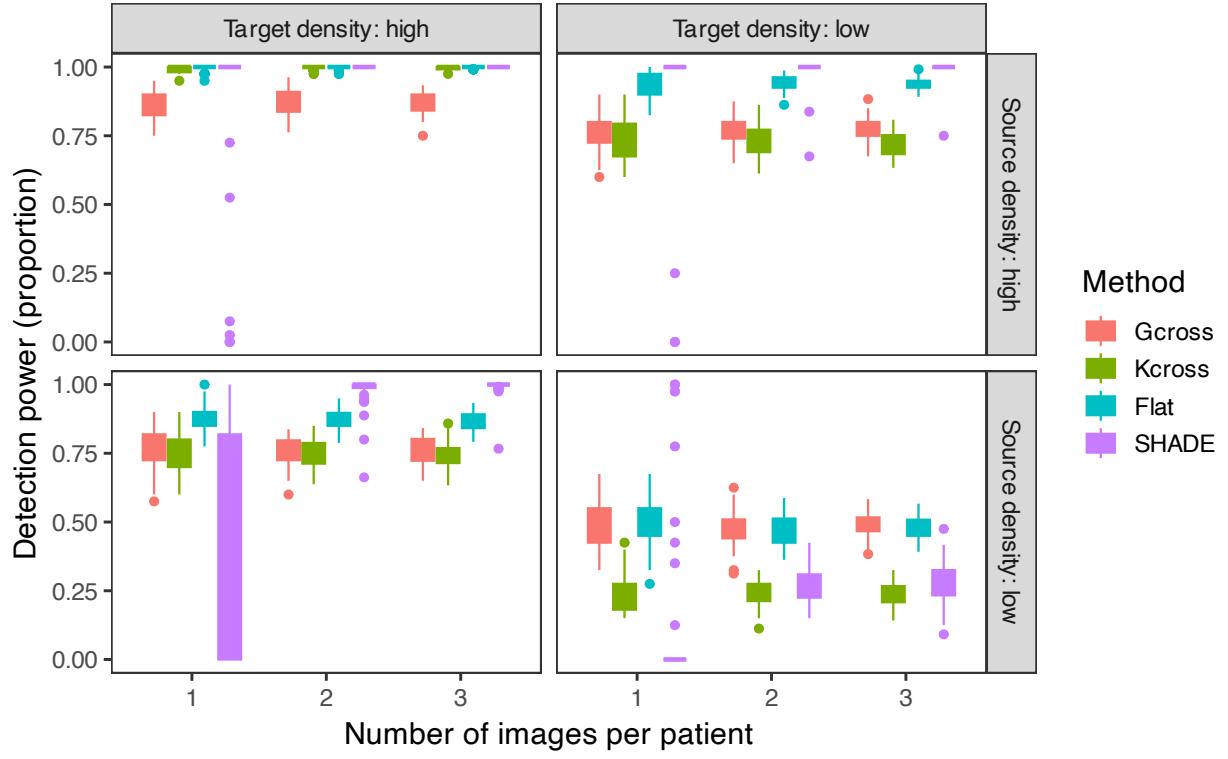
Figure 5: Detection power comparison across simulation conditions. Boxplots show the proportion of datasets in which methods correctly identify non-zero spatial interactions by testing whether simultaneous credible bands (SHADE) or global envelopes (G-cross, K-cross) exclude zero anywhere in the 0–75 μm range. Results are stratified by source cell density (rows: the conditioning cell type) and target cell density (columns: the cell type being modeled), with number of images per patient (1, 2, or 3) shown on the x-axis. SHADE Hierarchical achieves highest power when source density is high, with performance when source density is low depending critically on having multiple images per patient available for hierarchical pooling (see main text).
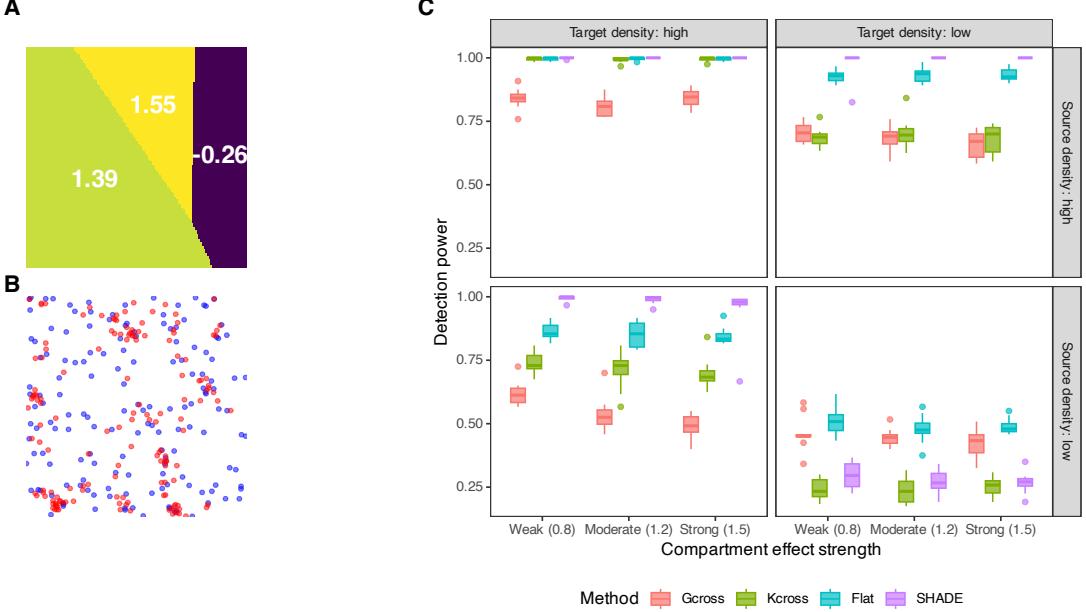
Figure 6: **Robustness to spatial confounding via compartments. A:** Compartment structure showing log-intensity effect on target density (3 compartments with moderate effect strength = 1.2). **B:** Example simulated pattern with tumor cells (red) and T cells (blue). **C:** Detection power stratified by compartment effect strength (weak/moderate/strong), source density (T cells, rows), and target density (tumor cells, columns). Despite unmeasured compartments, all methods maintain high power in favorable scenarios. However, elevated Type I error rates (see Supplement Section 3.10) indicate that SHADE incorrectly attributes compartment effects to source-target interactions when both cell types are abundant, demonstrating regime-dependent confounding bias.

4 Results: Multiscale inference of directional spatial interactions in colorectal cancer

4.1 Description of colorectal cancer dataset

We applied our hierarchical spatial interaction model to a publicly available colorectal cancer (CRC) dataset of multiplexed tumor tissue images from 35 patients [**?**]. The dataset includes four images per patient, each annotated with single-cell resolution across 16 cell types and 56 protein markers, yielding a multilevel structure of images nested within patients and patients nested within immune phenotype groups: Crohn's-like reaction (CLR) and diffuse

inflammatory infiltration (DII). CLR tumors are typically immune-infiltrated ("hot"), while DII tumors show immune exclusion ("cold").

For analysis, we focused on the eight most abundant cell types, including reclassification of "stroma" cells as hybrid epithelial-mesenchymal (E/M) cells and "smooth muscle" cells as cancer-associated fibroblasts (CAFs) based on marker expression [**??**]. Target populations were selected for their relevance to anti-tumor immunity (CD8$^+$ T cells, memory CD4$^+$ T cells, and granulocytes), while source populations included vasculature, tumor cells, CAFs, tumor-associated macrophages (TAMs, CD163$^+$), and hybrid E/M cells, reflecting key players in tissue architecture and immune regulation.

For each target cell type, we jointly estimated spatial interaction curves (SICs) with respect to all source types. Detailed data preparation procedures—including quadrature construction, basis function choices for interaction features, and model fitting settings—are provided in the Supplement.

4.2 How are specific cell types spatially organized in the tumor microenvironment?

A core question in tumor microenvironment analysis is whether certain cell types tend to cluster near or avoid others, and how these patterns vary with spatial scale. Such spatial relationships reflect underlying mechanisms of attraction, repulsion, communication, or physical constraint, and may provide insight into processes like immune surveillance, tumor evasion, and niche formation. SHADE's directional SICs allow detection of cell-type-specific clustering and exclusion behaviors across scales.

We extracted image-, patient-, and cohort-level interaction parameters ($\delta_{t_1 \to t_2}^{(m,p)}$, $\gamma_{t_1 \to t_2}^{(n,p)}$, and $\psi_{t_1 \to t_2}^{(g,p)}$) and computed SICs as in Equation 4. Figure 7 shows an example with cytotoxic T lymphocytes (CTLs, CD8$^+$ T cells) as the target cell type and CAFs as a source, highlighting differential organization between patient groups. At $\sim$75 μm, CTLs in CLR patients tend to cluster around CAFs (log-intensity > 0), whereas in DII patients, CTLs appear depleted

near CAFs. Patient-level curves reveal substantial within-group heterogeneity.

Across all cell-type pairs, we observed consistent short-range (<25 μm) negative associations, likely reflecting physical crowding (see figure in Supplement). At intermediate ranges (25–75 μm), many pairs showed a distinct positive peak, suggestive of clustering, often differing in magnitude between patient groups. Associations at longer distances (>75 μm) were generally weaker or absent, indicating limited spatial coordination at larger scales.
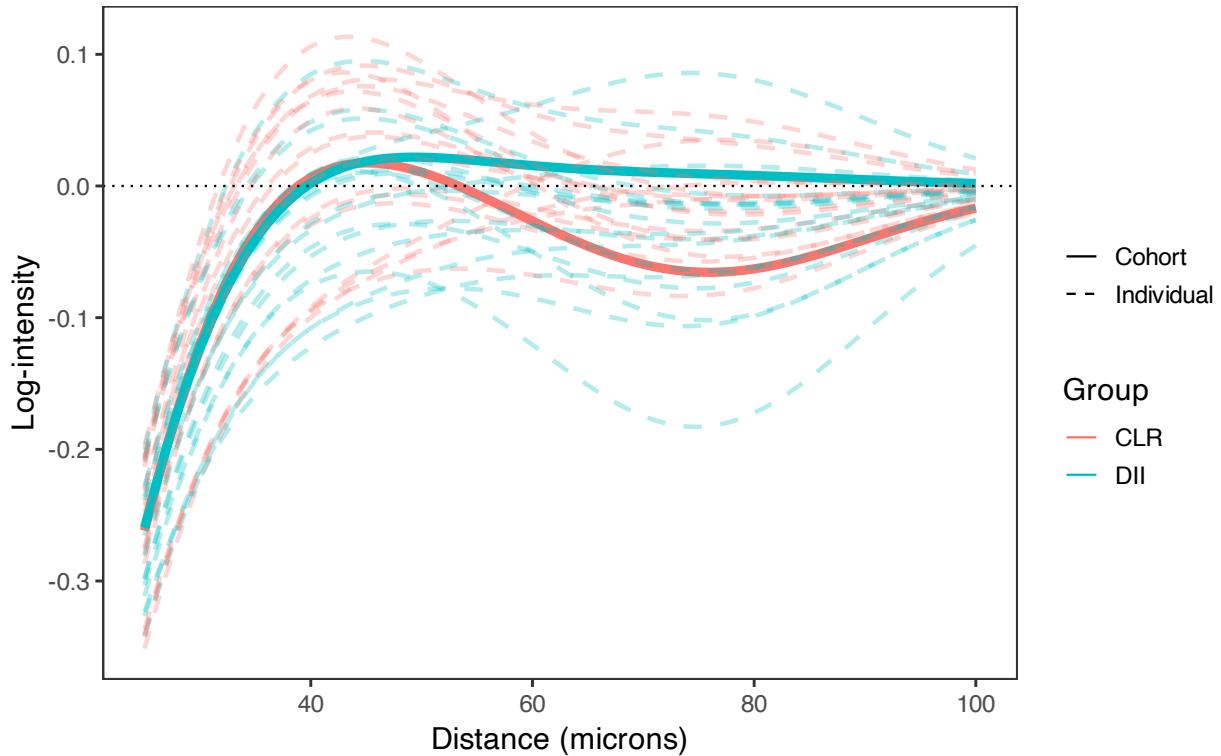
Figure 7: SIC showing the directional association of CAFs (source) with CTLs (target), stratified by patient group. Solid lines show cohort-level estimates for CLR and DII; dashed lines show patient-level SICs, illustrating hierarchical variability across patients within each cohort. CTLs in CLR patients exhibit midrange clustering around CAFs, while DII patients show neutral to avoidant patterns, indicating group-specific spatial organization.

4.3 How do spatial interaction patterns vary across patients and tissue sections?

Spatial interactions can vary across tumors and even between sections from the same patient, reflecting biologically meaningful heterogeneity in tumor architecture or immune organization. Unlike descriptive spatial statistics that compute separate summaries for each image, SHADE's hierarchical Bayesian model jointly estimates SICs at the image, patient, and cohort levels through partial pooling. This enables formal decomposition and quantification of variability at each biological scale, allowing us to assess both intra- and inter-patient variability and distinguish conserved from patient-specific spatial patterns .

To assess variability in spatial interaction structure across samples, we summarize between-patient and between-image heterogeneity using median absolute deviation (MAD)-based estimates. These measures are defined in the Supplement. Figure 8 shows heatmaps of the resulting variability estimates for each source–target cell type pair.
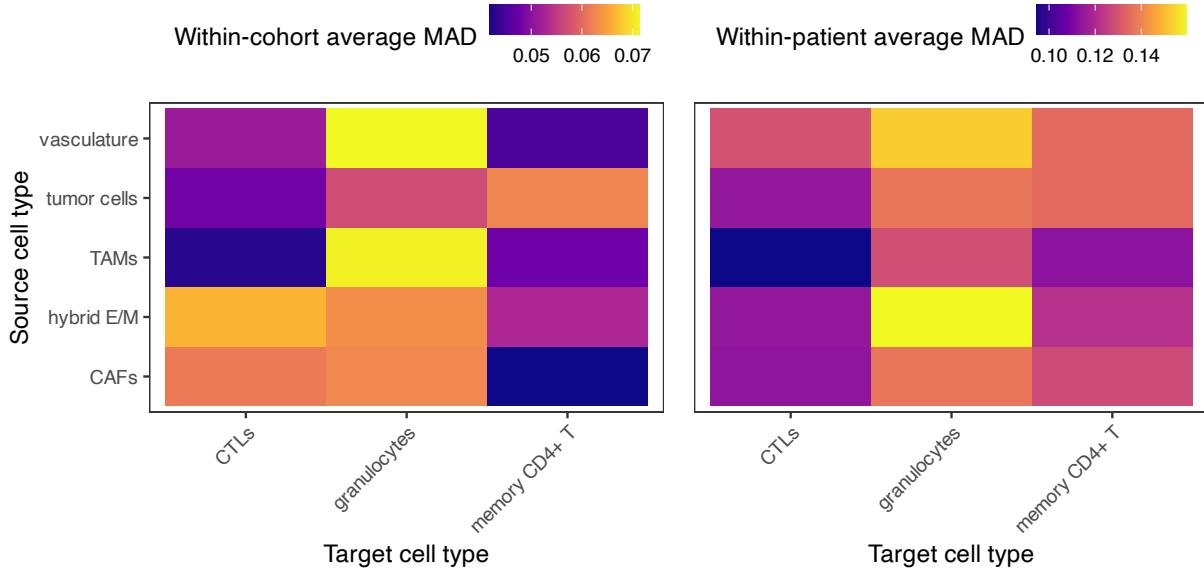

Figure 8: Heatmaps show the median absolute deviation (MAD) of SICs across spatial distances, summarizing two sources of variability: between patients (within cohort) and between images (within patient). Higher values indicate greater heterogeneity in spatial structure.

We observed substantial variability in spatial interaction structure across both patients and images (Figure 8). Notably, granulocytes clustering around TAMs and vasculature exhibited high between-patient heterogeneity. This suggests that granulocyte recruitment and localization near TAMs and vessels may be modulated by patient-specific microenvironmental states, such as differences in angiogenic signaling or myeloid activation. Within patients, granulocyte interactions also showed high heterogeneity, but principally in association with vasculature and hybrid E/M cells. These image-level differences may reflect localized fluctuations in endothelial activation or epithelial plasticity, which may differentially attract or retain granulocytes within specific tissue regions. Examples of patient-level curves for two patients, along with their image-level curves, are shown in Figure 9.

Comparing heterogeneity patterns between CLR and DII tumor subtypes reveals subtype-specific differences in variability (Supplement Figure S21). At the patient level, DII tumors show greater between-patient heterogeneity than CLR tumors for several immune-related interactions, most notably memory CD4+ T cells with CAFs (MAD difference = 0.015), CTLs with tumor cells (0.014), and granulocytes with vasculature (0.014). Conversely, CLR tumors exhibit greater between-patient variability for granulocyte-CAF interactions (MAD difference = −0.025) and memory CD4+ T-TAM interactions (−0.017). At the image level, DII tumors show more within-patient heterogeneity for granulocyte-vasculature (MAD difference = 0.028) and memory CD4+ T-tumor interactions (0.017), while CLR tumors show greater within-patient variability for granulocyte interactions with hybrid E/M cells (−0.034) and CAFs (−0.031), and for CTL-CAF interactions (−0.020). These results demonstrate that tumor subtype affects not only the mean spatial interaction patterns (Section 4.4) but also their variability at both between-patient and within-patient scales. The particularly strong subtype-specific differences in granulocyte-related heterogeneity may reflect distinct modes of myeloid cell recruitment and spatial organization between the two tumor subtypes.
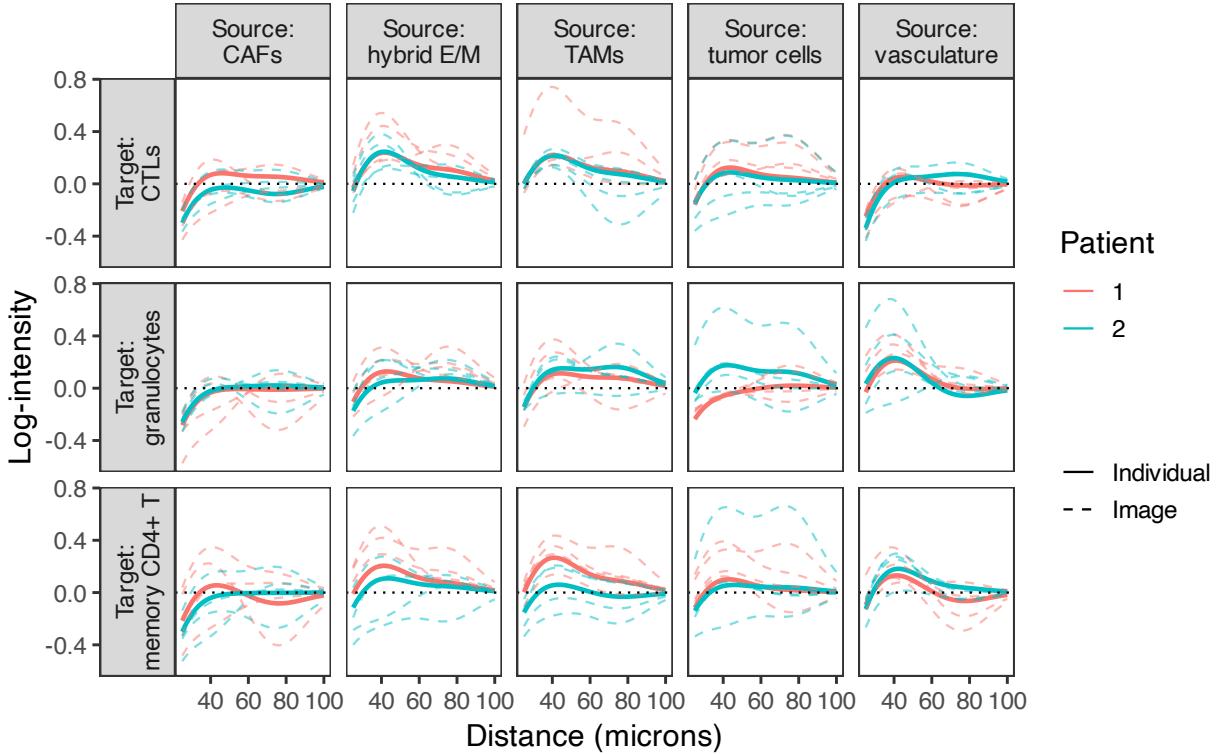
Figure 9: Examples of patient- and image-level SICs for cell type pairs with high within-patient MAD values. Solid lines show patient-level SICs; dotted lines show image-level SICs from individual tissue sections, illustrating hierarchical variability within patients.

4.4 How do immune and stromal spatial interactions differ between hot and cold tumors?

Distinct tumor immune phenotypes—such as immune-infiltrated versus immune-excluded tumors—are associated with differential immune activity and prognosis. These differences are often accompanied by changes in how immune and stromal cells are spatially arranged in relation to tumor cells and each other. We used SHADE to compare SICs across these patient groups and identify interactions that are enriched or depleted in each context. This allowed us to link differences in spatial structure to known functional differences in immune activity.

We observed several notable differences in SICs between CLR and DII patients (Figure 10). Below, we highlight a subset of interactions where the between-group difference

in log-intensity exceeds 0.05 (dashed lines in Figure 10), focusing on plausible underlying biological mechanisms. First, CLR patients showed increased clustering of CTLs and memory CD4+ T cells around vasculature at short spatial ranges, suggesting enhanced immune surveillance and trafficking in these patients. The vasculature serves as a conduit for lymphocyte infiltration into the tumor microenvironment, and vascular normalization in immunologically active tumors has been linked to improved T cell recruitment and anti-tumor immunity [??]. This may reflect a more organized immune response in CLR patients, consistent with better clinical outcomes. In contrast, DII patients exhibited greater clustering of CTLs around tumor cells at all spatial ranges. While this might suggest immune recognition, it may alternatively indicate ineffective or exhausted T cell responses that fail to clear tumor cells. Persistent CTL-tumor colocalization without effective cytolysis has been associated with immune dysfunction and tumor immune escape [??].

We also observed distinct patterns in CTL clustering around CAFs: DII patients displayed increased clustering at short and long spatial ranges, whereas CLR patients showed elevated clustering at medium ranges. CAFs are known to mediate immune suppression via direct inhibition of CTLs and by establishing physical and cytokine-mediated barriers [??]. The long-range clustering in DII patients may reflect exclusionary barriers or CAF-mediated trapping of CTLs, whereas the medium-range interactions in CLR patients could represent transient engagement or immune cell penetration into CAF-dense zones under less suppressive conditions. Lastly, CLR patients demonstrated increased clustering of memory CD4+ T cells at short distances from both CAFs and hybrid E/M cells. This may suggest spatial niches where helper T cells coordinate localized immune responses, potentially promoting anti-tumor immunity or influencing the differentiation state of tumor cells. CD4+ T cells have been implicated in the modulation of EMT processes, and their proximity to hybrid E/M cells may reflect attempts to restrain phenotypic plasticity and metastatic potential [??].

27
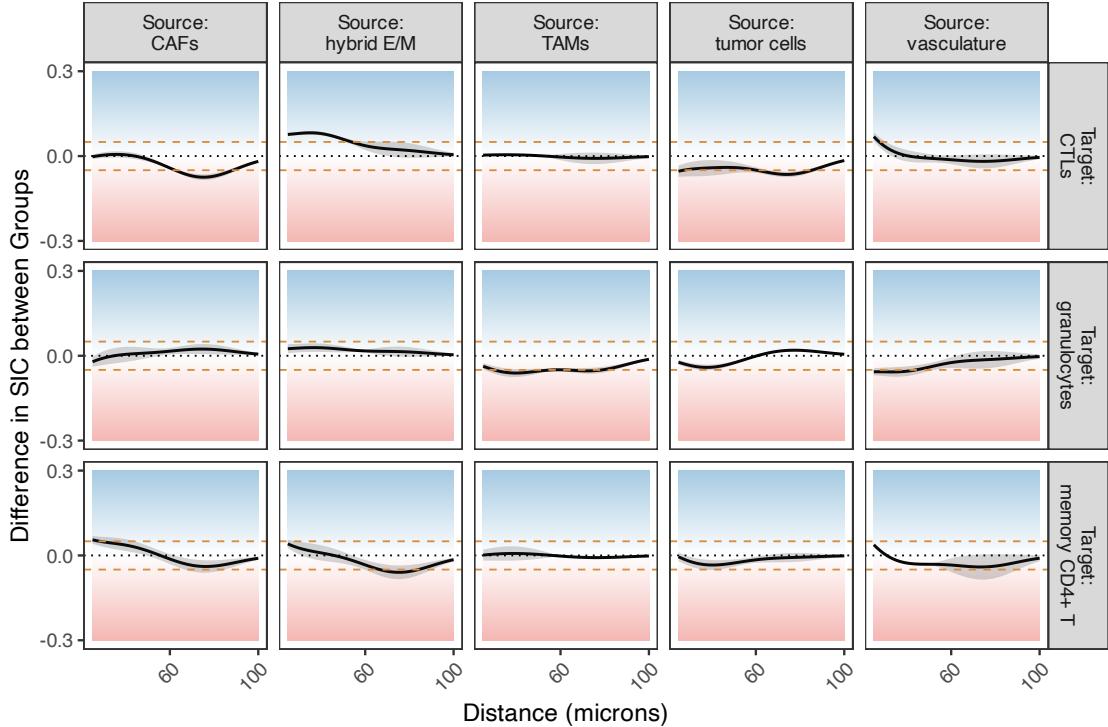
Figure 10: The difference in SICs between the two patient groups, with simultaneous 95% credible bands. Curves above 0 (in the blue area) indicate that the log-intensity is greater in CLR patients than DII patients; curves in the red area show the reverse.

4.5 How well can spatial interactions predict the organization of individual cell types across tumor regions?

Beyond estimating SICs, SHADE predicts the spatial distribution of each target cell type conditional on the source cells, allowing us to assess how well spatial interactions explain observed patterns. This reveals which cell types are more spatially constrained and how predictability varies across images, patients, and tumor subtypes.

For example, in image 47_B from the dataset, we can produce the following predictions of each target cell type, conditional on the source cell types (Figure 11). We can see that the target cell types are quite well predicted, especially CTLs. Likely due to their relative paucity, granulocytes are not quite as well predicted in this image (regions of localization are not as distinct).

We calculated AUCs per cell type and per group (see Supplement). All three target

cell types were better predicted in CLR patients than in DII patients, though there was a relatively large amount of variability in image-level AUCs.
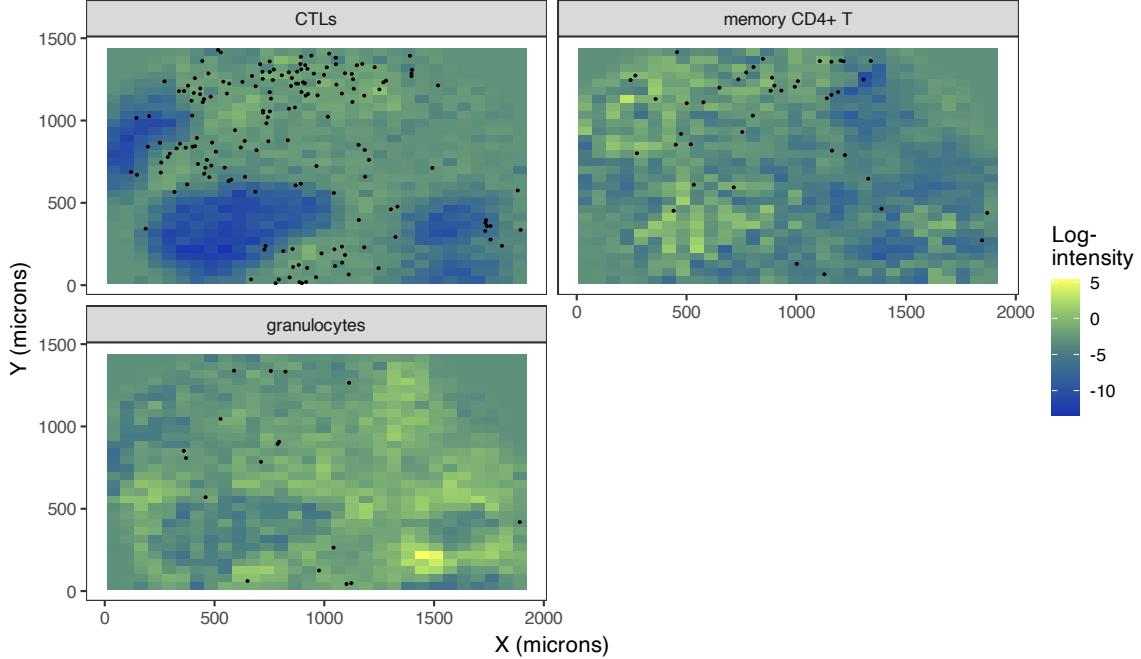

Figure 11: Predicted spatial distributions for target cell types in a representative image (47_B), based on the estimated conditional intensity functions. Heat maps show predicted log-intensity; black dots indicate observed cell locations for each target cell type.

4.6 Comparing SHADE to traditional G-cross-based spatial clustering analysis

To contextualize our SHADE results, we performed an alternative analysis using the G-cross function [?], a nonparametric estimator of cross-type clustering commonly used in spatial point pattern analysis. This comparison highlights how SHADE differs from traditional methods in its modeling framework and interpretability of results.

For each tissue section, we computed G-cross estimates at distances from 0 to 80 microns and extracted values at key distances (20, 40, 60 microns) for comparison. To quantify whether differences in clustering could predict patient group (CLR vs DII), we fitted logistic regression models with G-cross as the predictor and used FDR-adjusted p-values to identify

29

significant associations. The resulting estimates are visualized as a heatmap of log-odds ratios (log-ORs), indicating the strength and direction of group differences in clustering at each distance.
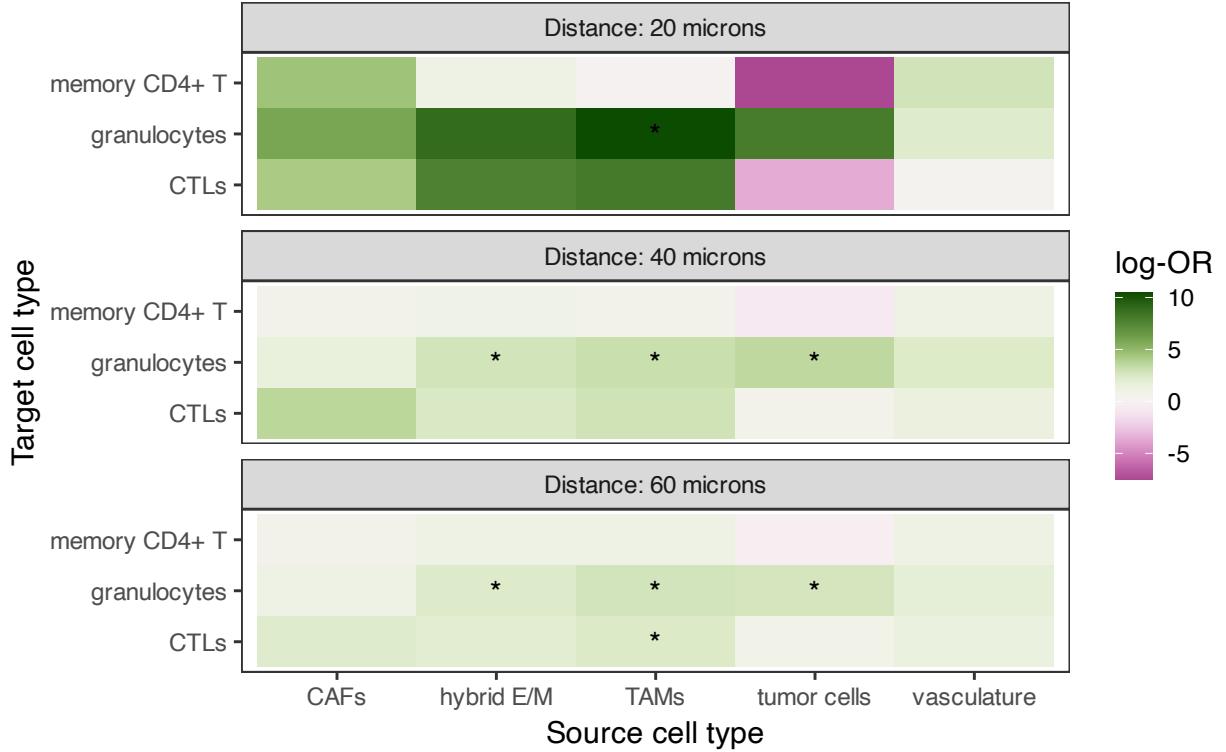

Figure 12: Heatmap of log-odds ratios (log-ORs) from logistic regression models comparing G-cross clustering metrics between CLR and DII patient groups, stratified by distance (20, 40, 60 microns). Tiles represent the estimated log-OR for each source–target pair at a given distance, with asterisks indicating significant differences ($p < 0.05$, FDR-adjusted). Green indicates stronger clustering in DII, purple indicates stronger clustering in CLR.

The G-cross-based analysis (Figure 12) reveals several patterns of cell–cell clustering between CLR and DII patients, but notable differences emerge when we compare these results with SHADE-derived SICs. For instance, TAM–granulocyte interactions showed strong, statistically significant differences at all examined distances (20–60 microns), with higher clustering in DII tumors. This suggests a prominent granulocyte-TAM association in DII tumors according to G-cross. However, SHADE did not highlight this pair as a major differential interaction between groups, indicating that the clustering of granulocytes around TAMs may not translate into strong directional interactions when adjusting for other cell

types or when modeled hierarchically. Conversely, SHADE identified vasculature as a key source driving differences in clustering of both CTLs and memory CD4+ T cells between CLR and DII groups, reflecting enhanced immune surveillance or trafficking around blood vessels in CLR tumors. This vasculature effect is less evident in the G-cross analysis, where vasculature-related interactions showed limited significance and mostly small effect sizes. These discrepancies highlight how SHADE's joint modeling and multilevel structure may capture spatial dependencies missed by simpler summary statistics like G-cross, or may reduce confounding by accounting for other cell types and hierarchical data structure. Conversely, G-cross may capture strong pairwise clustering that SHADE's model de-emphasizes in favor of more complex or conditional dependencies. Overall, this comparison underscores the differences in what each method captures, emphasizing SHADE's ability to reveal nuanced, context-dependent spatial interactions.

4.7 Visual comparison with functional data analysis of spatial summary statistics

To provide additional context for SHADE's results and explore complementary perspectives on group-level spatial organization, we compared SHADE's group-level SICs with functional data analysis (FDA) of marginal pairwise summary statistics. Specifically, we applied multilevel functional principal component analysis (mFPCA) [?] separately to CLR and DII patient groups, analyzing G-cross and L-cross functions computed for each tissue section.

Unlike SHADE, which models conditional intensities adjusting for all cell types simultaneously within a generative point process framework, mFPCA decomposes functional variation in observed summary statistics across hierarchical levels (images nested within patients). This approach does not provide a probabilistic model of the underlying point process, but instead characterizes dominant modes of variation in the empirical G-cross and L-cross curves. The resulting group-level mean functions with uncertainty bands (mean $\pm$ 1 SD from the first functional principal component) provide a complementary view of pairwise spatial as-

sociations.

We computed G-cross and L-cross functions for all 15 source-target pairs at distances from 0 to 75 μm, ran mFPCA separately for each group (pve = 0.99), and extracted the population mean curves with variability bands. Full mFPCA results for all pairs are provided in the Supplement (Figures S[#] and S[#] for G-cross and L-cross, respectively). Visual comparison of SHADE SICs (Figure 10) with mFPCA group curves reveals both concordance and informative differences.

For instance, SHADE identified vasculature as driving increased short-range clustering of CTLs in CLR patients (Figure 10). The G-cross mFPCA analysis shows qualitatively similar patterns, with CLR patients exhibiting lower G-cross values at short distances (indicating clustering) compared to DII patients. This concordance suggests that SHADE's conditional modeling captures genuine marginal pairwise associations for this interaction. Conversely, for CTL-tumor cell interactions, SHADE detected elevated clustering in DII patients across all distances, while G-cross mFPCA curves show more subtle group differences with overlapping uncertainty bands at intermediate distances. This discrepancy may reflect SHADE's multivariate adjustment—controlling for other cell types reveals stronger directional effects than marginal pairwise statistics suggest.

This comparison illustrates the complementary nature of SHADE and FDA approaches: SHADE's conditional modeling isolates directional effects while adjusting for confounders, whereas mFPCA characterizes marginal pairwise variation without multivariate adjustment. Both perspectives contribute to understanding group-level spatial organization in the tumor microenvironment.

5   Discussion

In this work, we introduced SHADE, a Bayesian hierarchical model for quantifying asymmetric spatial interactions in multiplexed imaging data. By modeling the conditional intensity

function and estimating spatial interaction curves, our approach enables the identification of directional associations between cell types while accounting for multilevel variation across images, patients, and cohorts.

Through simulation studies, we demonstrated that SHADE effectively captures asymmetric spatial associations while leveraging hierarchical structure to improve estimation. Including multilevel priors improves inference accuracy, especially for short-range interactions, by reducing bias and variance in estimated coefficients. SHADE also demonstrated superior robustness to low cell densities and limited sampling, consistently outperforming G-cross and flat models in detecting true spatial interactions across diverse simulation conditions.

A key advantage of SHADE over traditional spatial summary statistics is its ability to formally model and quantify heterogeneity across biological scales. While methods such as Ripley's K-function and the G-cross function can compute separate estimates for each image and then compare them post-hoc, SHADE's hierarchical Bayesian framework enables joint estimation with partial pooling, explicit variance decomposition, and formal quantification of between-patient and within-patient variability (Section 4.3). This distinction is crucial for biomedical datasets where spatial patterns exhibit systematic variation across patients and tissue sections, and where borrowing strength across the hierarchy improves estimation efficiency and enables more nuanced biological inference.

SHADE revealed distinct and biologically meaningful patterns of cellular organization in colorectal tumors, highlighting how immune and stromal interactions differ between immune-infiltrated (CLR) and immune-excluded (DII) phenotypes. By estimating directional spatial interaction curves across multiple spatial scales and model hierarchies, we identified key differences in the local microenvironment that may underlie divergent immune states. Notably, CLR tumors exhibited increased short-range clustering of cytotoxic and memory T cells around vasculature, consistent with enhanced immune infiltration via normalized vessels and the formation of perivascular immune niches. In contrast, CTLs in DII tumors showed elevated spatial association with tumor cells across all distances—a pattern that may reflect

either failed immune surveillance or dysfunctional retention of exhausted T cells.

Our analysis also uncovered cell-type-specific interaction patterns with stromal components. CTLs in DII patients showed greater clustering near CAFs at both short and long spatial ranges, whereas in CLR patients, CTL–CAF interactions peaked at intermediate distances. Given CAFs' established role in immune suppression and physical exclusion, these patterns may reflect differential stromal constraint across tumor types. Similarly, CLR patients exhibited increased short-range clustering of memory CD4+ T cells around both CAFs and hybrid E/M cells. These interactions suggest a potentially immunoregulatory or anti-tumor role for helper T cells in CLR tumors, possibly including modulation of EMT plasticity or the stabilization of immune-supportive niches.

Beyond cohort-level differences, we also found substantial heterogeneity in spatial organization across patients and across tissue sections from the same patient. This variability was particularly pronounced in granulocyte interactions with TAMs, vasculature, and hybrid E/M cells, suggesting patient-specific or localized microenvironmental factors influencing spatial localization. Finally, SHADE's ability to predict target cell distributions from spatial covariates varied by cell type and tumor subtype: immune cell organization was more predictable in CLR tumors, indicating more structured immune environments compared to the more disorganized spatial context of DII tumors. Collectively, these results emphasize the need for multiscale spatial modeling to capture both consistent interaction motifs and the biologically meaningful variability that characterizes tumor immune landscapes.

Additionally, we compared SHADE's results with G-cross function estimates, a standard spatial summary statistic. G-cross estimates identified strong clustering of granulocytes around TAMs and hybrid E/M cells, which SHADE did not highlight. Conversely, SHADE revealed significant vasculature-driven clustering of CTLs and memory CD4+ T cells in CLR tumors, a pattern less evident in G-cross estimates. This highlights how SHADE's hierarchical, conditional modeling framework can capture context-dependent interactions that simpler pairwise clustering methods might miss or misrepresent.

Our comparison with multilevel functional PCA (Section 4.7) further illustrates the complementary strengths of SHADE and functional data analysis approaches. While both methods analyze spatial patterns hierarchically, they address fundamentally different questions: SHADE provides a generative probabilistic model of the point process with multivariate adjustment for confounding cell types, whereas mFPCA characterizes dominant modes of variation in marginal pairwise summary statistics without imposing a parametric model on the underlying spatial process. The concordance we observed between SHADE's conditional SICs and mFPCA's marginal G-cross curves for certain interactions (e.g., CTL-vasculature) validates that SHADE's directional effects reflect genuine pairwise spatial associations. Conversely, discrepancies highlight where multivariate adjustment reveals conditional dependencies not apparent in marginal analyses. This suggests that SHADE and FDA methods are best viewed as complementary tools rather than competing approaches: SHADE excels at isolating directional causal effects while controlling for confounders, whereas FDA methods provide model-free exploration of functional variation across biological hierarchies. The choice between approaches should be guided by the inferential goal—mechanistic understanding of conditional dependencies versus descriptive characterization of marginal spatial patterns.

A key strength of SHADE is its flexibility in modeling directional interactions across spatial scales, avoiding the restrictive symmetry assumptions of traditional spatial models. Moreover, the use of logistic regression for conditional intensity estimation allows for scalable and stable inference, sidestepping common numerical pitfalls of direct Poisson modeling.

Nonetheless, SHADE has limitations. First, while SICs capture directional spatial association, they remain correlational and cannot determine causality or infer mechanisms of interaction. Second, the SICs reflect spatial dependence rather than molecular signaling pathways, which may limit biological interpretability in some settings. Third, although SHADE supports biologically motivated conditioning structures, exploratory analyses may benefit from modeling both directions of association when directionality is uncertain.

Future extensions of SHADE could incorporate functional covariates—such as marker intensity, proliferation, or exhaustion scores—into the SIC framework, enabling joint analysis of spatial structure and functional state. This would open the door to modeling not just where cells are, but how they behave spatially in context. Additionally, where cell segmentation boundaries are available, boundary-to-boundary distances could be used in place of centroid-to-centroid distances, further reducing geometric crowding effects at short spatial ranges and improving biological interpretability of near-contact interactions.

Overall, our results highlight the importance of capturing asymmetric and hierarchical structure in spatial models, and position SHADE as a powerful tool for dissecting the complex architecture of tissue microenvironments in cancer and beyond.

Acknowledgements

Conflict of Interest

Funding